

# Deterministic Guidance Diffusion Model for Probabilistic Weather Forecasting

Donggeun Yoon\*  
Chungnam National University  
ehdrms903@gmail.com

Minseok Seo\*  
SI Analytics  
minseok.seo@si-analytics.ai

Doyi Kim  
SI Analytics  
doyikim@si-analytics.ai

Yeji Choi  
SI Analytics  
yejichoi@si-analytics.ai

Donghyeon Cho<sup>†</sup>  
Chungnam National University  
cdh12242@gmail.com

## Abstract

Weather forecasting requires not only accuracy but also the ability to perform probabilistic prediction. However, deterministic weather forecasting methods do not support probabilistic predictions, and conversely, probabilistic models tend to be less accurate. To address these challenges, in this paper, we introduce the **Deterministic Guidance Diffusion Model (DGDM)** for probabilistic weather forecasting, integrating benefits of both deterministic and probabilistic approaches. During the forward process, both the deterministic and probabilistic models are trained end-to-end. In the reverse process, weather forecasting leverages the predicted result from the deterministic model, using as an intermediate starting point for the probabilistic model. By fusing deterministic models with probabilistic models in this manner, DGDM is capable of providing accurate forecasts while also offering probabilistic predictions. To evaluate DGDM, we assess it on the global weather forecasting dataset (WeatherBench) and the common video frame prediction benchmark (Moving MNIST). We also introduce and evaluate the Pacific Northwest Windstorm (PNW)-Typhoon weather satellite dataset to verify the effectiveness of DGDM in high-resolution regional forecasting. As a result of our experiments, DGDM achieves state-of-the-art results not only in global forecasting but also in regional forecasting. The code is available at: <https://github.com/DongGeun-Yoon/DGDM>.

## 1. Introduction

Weather is a critical variable that impacts various aspects of daily life, including aviation, logistics, agriculture, and transportation. To provide accurate weather forecasting, the numerical weather prediction (NWP) method has been

\*equal contribution

<sup>†</sup>corresponding author

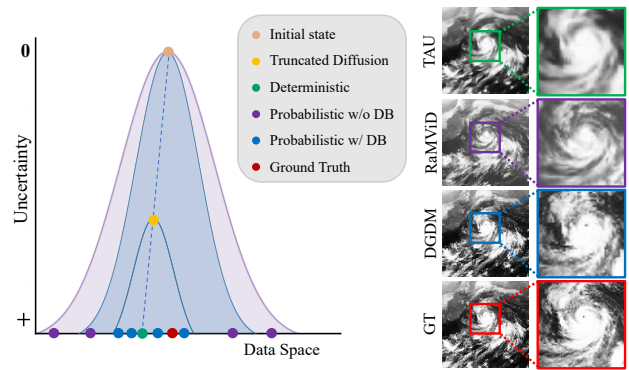


Figure 1. Comparison of uncertainty between probabilistic (RaMViD) and deterministic (TAU) models. The probabilistic model exhibits high diversity, making sample selection near GT challenging. On the other hand, the deterministic model produces a single output, which limits its ability to capture real-world weather variability and constrains its practical application.

predominantly used for most weather forecasting since the 1950s [5, 7]. NWP employs a simulation-centric framework with vertical and horizontal grids (usually between 10 km and 25 km) that divide the Earth’s atmosphere. Each grid cell translates the governing atmospheric behavior into partial differential equations (PDEs), which are then solved using numerical integral methods. Even a single 10-day forecast simulation with the NWP model requires hours of computation on hundreds of supercomputer nodes. Despite these efforts, phenomena such as turbulent motion and tropical cumulus convection, which occur on a scale of a few kilometers horizontally, cannot be captured by a single deterministic prediction due to being smaller than the grid of NWP models. Also, the nonlinearity or randomness of atmospheric phenomena makes it difficult to conduct accurate simulations [19].

Therefore, NWP models add small random perturbations to the initial weather conditions and perform multiple sim-

ulations to consider the possible scenarios. This ensemble forecasting effectively represents unpredictable events due to nonlinearity or randomness inherent in atmospheric phenomena. However, it is difficult to configure many ensemble members for the NWP model, which requires a huge amount of computation and time to generate a single prediction.

To alleviate these problems of the NWP model, several data-driven weather forecasting approaches have been proposed [3, 20]. While all have surpassed the performance of NWP in 10-day global weather forecasting, they are fundamentally deterministic models and therefore fail to capture the subgrid-scale process<sup>1</sup>. Recently, probabilistic weather forecasting models [9, 21] using latent diffusion models have been proposed to predict plausible multiple future weather conditions. They have successfully performed data-driven probabilistic weather forecasting, but due to their diversity, it is unclear which of the various samples should be selected, or ensemble methods may actually degrade performance. Therefore, data-driven weather forecasting faces a trade-off problem where deterministic models have high performance but cannot perform probabilistic prediction, and probabilistic models generate diverse samples but with lower accuracy.

In this paper, we introduce a **Deterministic Guidance Diffusion Model (DGDM)** for probabilistic weather forecasting. As shown in Figure 1, weather forecasting using diffusion processes presents challenges, particularly because of the inherent variability in diffusion methods. This variability can lead to the selection of samples that deviate significantly from the ground truth. On the other hand, deterministic models tend to include all possible futures, resulting in a single and ambiguous outcome. DGDM addresses the challenges by integrating both deterministic and probabilistic models. DGDM is structured into two branches: deterministic and probabilistic, as shown in Figure 2. During the training phase, the deterministic branch takes the initial weather condition, denoted as  $x$ , as its input and aims to minimize discrepancies with the future weather condition  $y$ . Simultaneously, the probabilistic branch uses both the initial weather condition  $x = x_T$  and the future weather condition  $y = x_0$  to train a direct mapping between the domains, using a Brownian bridge stochastic process. Here,  $T$  represents a diffusion process step. Subsequently, during the inference phase, the forecast from the deterministic branch serves as an intermediate starting point for the stochastic model, integral to the truncated diffusion process. In particular, by adjusting the starting point of the reverse process, DGDM addresses the inherent uncertainty of weather forecasting, allowing it to control the range of

<sup>1</sup>**Subgrid-Scale Process:** Atmospheric processes occurring at the smallest scales cannot be represented deterministically within a numerical simulation ([4]).

possible future weather scenarios.

To verify its efficacy in high-resolution regional weather forecasting, we introduce and evaluate it using the Pacific Northwest Windstorm (PNW)-Typhoon weather satellite dataset. In addition, We validate DGDM for low-resolution global weather forecasting using the WeatherBench dataset. Lastly, to determine its effectiveness not only in weather forecasting but also in general video frame prediction, we assess it on the widely used Moving MNIST dataset. Our evaluation results show that DGDM not only achieves state-of-the-art performance in low-resolution global weather forecasting and high-resolution regional weather forecasting but also demonstrates high performance in the Moving MNIST video frame prediction task.

## 2. Related Work

### 2.1. Data-driven Weather Forecasting

Data-driven weather forecasting is gaining significant attention for providing accuracy comparable to NWP models even without supercomputing resources. In particular, in many countries where supercomputers cannot be operated, data-driven weather forecasting is a new paradigm that can perform weather forecasting with a single GPU server.

DGMR [27] employed a generative adversarial training approach, utilizing both temporal and spatial discriminators separately. Shi *et al.* [32] introduced a ConvLSTM to predict precipitation via autoregressive inference. Furthermore, Ayzel *et al.* [1] and Trebing *et al.* [36] presented a data-driven short-term precipitation forecasting leveraging the U-Net architecture [11, 29]. Beyond precipitation, studies such as [3, 6, 20] have proposed data-driven models for forecasting global climate variables. The Fourier-based neural network model [6] was designed to generate global data-driven forecasting for atmospheric variables. Subsequently, models such as GraphCast [20] and Pangu-Weather [3] have outperformed NWP in 10-day forecasts. While there have been significant advancements, these data-driven forecasting models are deterministic. This means that they cannot represent nonlinear and random subgrid-scale phenomena.

### 2.2. Video Frame Prediction

Video frame prediction has various applications such as weather forecasting [11], human motion prediction [18], traffic flow prediction [42] and human robot interaction [8]. Video frame prediction is primarily divided into two main categories: autoregressive and non-autoregressive methods. Traditionally, autoregressive techniques, employing architectures such as ConvLSTM [32] and RNN [12, 38, 39], have been foundational in the field of video frame prediction. Notably, PhyDNet was introduced in [12], which consists of a two-branch deep architecture designed to disen-

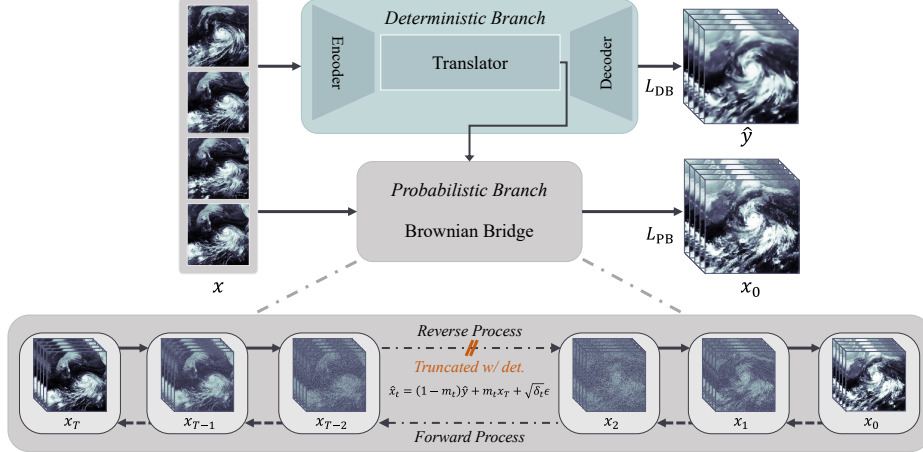


Figure 2. Overview of DGDM: During training, DGDM simultaneously trains both the deterministic and probabilistic models. During inference, the results of the deterministic model are used to truncate the reverse process of the probabilistic model.

tangle physical dynamics from unknown factors. PhyD-Net achieved state-of-the-art performance across multiple datasets through a recurrent physical cell (PhyCell) that executes PDE-constrained prediction in a latent space. Despite various advancements, autoregressive models inherently suffer from deteriorating performance due to errors accumulation with increasing lead time.

To tackle the problem of error accumulation inherent in autoregressive models, recent research has turned towards non-autoregressive approaches [10, 17, 24, 30, 34, 43]. For instance, Gao *et al.* [10] designed a non-autoregressive model featuring a multi-in-multi-out structure called SimVP, to prevent error accumulation over specified target lead times. However, most video frame prediction models were developed based on minimizing the mean squared error (MSE) between predictions and ground truth, which is unsuitable for probabilistic weather forecasting.

### 2.3. Video Generation

Video generation technology has made great progress by applying a variety of approaches, including GAN [23], VAE [2, 25], and diffusion models [15, 16, 37]. Especially after denoising diffusion probabilistic models (DDPM) [14], there has been notable progress in the video generation field. Ho *et al.* [15] proposed a video diffusion model (VDM) that generates videos by gradually denoising noisy videos. VDM is trained to maximize the variational lower bound of the log-likelihood of the data and achieves impressive results on various video-related tasks, such as video generation, editing, and compression. Afterward, RaMViD [16], which proposed random-mask video diffusion, and MCVD [37], which integrated video prediction, generation, and interpolation into one framework, were proposed. While these probabilistic models can gen-

erate plausible future frames, they are not optimized for accurate predictions.

Therefore, simply applying video generation models to weather forecasting is unsuitable for expressing uncertainty because they cannot control their diversity. The proposed DGDM addresses this issue by effectively merging probabilistic and deterministic models, offering a probabilistic model that can still control the range of possible future weather scenarios.

## 3. Method

The objective of DGDM is to forecast future weather condition  $y \in \mathbb{R}^{C \times \hat{L} \times H \times W}$  given the initial weather condition  $x \in \mathbb{R}^{C \times L \times H \times W}$ . Where  $H$ ,  $W$ , and  $C$  represent the height, width, and channels, respectively.  $L$  and  $\hat{L}$  denote the lengths of the observed and forecasted frames. As shown in Figure 2, DGDM consists of two main components: the deterministic branch and the probabilistic branch. The probabilistic branch accounts for the inherent uncertainties in future forecasting, ensuring a wide range of possible futures. On the other hand, the deterministic branch improves the accuracy of forecasts. Furthermore, the results from the deterministic branch are used to modulate uncertainties, which in turn helps to control the diversity of potential future weather scenarios in the probabilistic branch.

### 3.1. Deterministic Branch

The deterministic branch (DB) of the DGDM adopts a non-autoregressive structure, which is beneficial for achieving high performance as it prevents error accumulation at fixed lead times. The model architecture consists of an encoder  $e(\cdot)$ , a translator  $st(\cdot)$ , and a decoder  $d(\cdot)$ , similar to the structure utilized in TAU [34]. Given an input  $x$ , the loss

function of the deterministic branch is formulated as:

$$L_{DB} = \|y - d(st(e(x)))\|^2. \quad (1)$$

### 3.2. Probabilistic Branch

The probabilistic forecasting method in NWP is to apply different small random perturbations to the initial conditions each time the model is run, thereby generating diverse outcomes. Inspired by the NWP process, which produces probabilistic predictions through deterministic start and end points coupled with perturbations to the initial conditions, the probabilistic branch of the DGDM has been designed.

**Brownian Bridge Diffusion Process** When we consider the problem as one of predicting the stochastic trajectories between an initial weather condition  $x$  and a future weather condition  $y$ , a Brownian bridge can be applied as a continuous-time stochastic model where the probability distribution during the diffusion process is conditional on the starting and ending states. Specifically, the state distribution at each time step of a Brownian bridge process starting from point  $y = x_0$  with  $x_0 \sim q_{\text{data}}(x_0)$  at  $t = 0$  and ending at point  $x = x_T$  at  $t = T$  can be formulated as:

$$p(x_t|x_0, x_T) = \mathcal{N}\left(\left(1 - \frac{t}{T}\right)x_0 + \frac{t}{T}x_T, \frac{t(T-t)}{T}\mathbf{I}\right), \quad (2)$$

where  $\mathcal{N}$  denotes the normal distribution and  $\mathbf{I}$  is the identity matrix that scales the variance of the distribution.

We can define the Brownian bridge diffusion process in the simplified notation of DDPM as follows:

$$q(x_t|x_0, x_T) = N(x_t; (1 - m_t)x_0 + m_tx_T, \delta_t I), \quad (3)$$

$$x_0 = y, m_t = \frac{t}{T}.$$

Note that, as in the case of image to image translation tasks where the Brownian bridge diffusion process has been successfully applied [22], in DGDM,  $\delta_t$  is defined as  $2(m_t - m_t^2)$ .

#### Deterministic Guidance Diffusion Model for Probabilistic Weather Forecasting

The structure of the probabilistic branch (PB) of DGDM is modeled after VDM [15]. Unlike VDMs that generate video clips from noise, PB applies Eq. (3) when given input  $x$  and output  $y$ . However, using input  $x$  directly leads to two main issues. First, the length of input  $L$  must match the target length  $\hat{L}$  for the diffusion model to function properly, which complicates the control of output length  $\hat{L}$ . Second,  $x^0$ , the first frame of the input, has the greatest lead time distance from the first frame of the target  $y^0$ . In contrast,  $x^L$  is closer to  $y^0$ , where the superscript number denotes the specific frame. This makes the direct use of  $x$  to perform Eq. (3) inefficient. To address

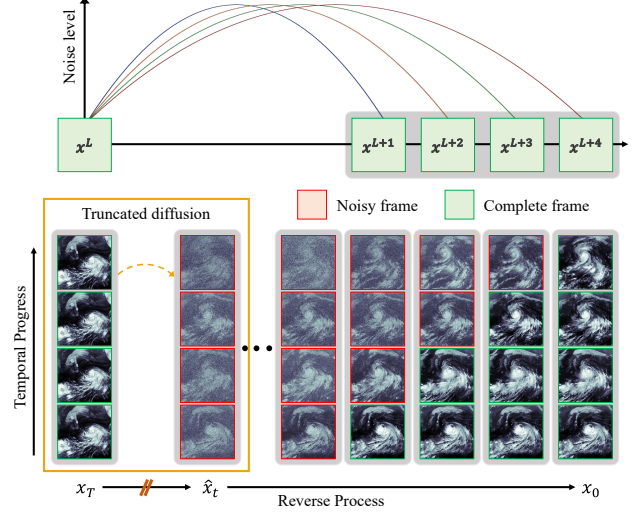


Figure 3. The reverse process of DGDM employs the sequential variance schedule (SVS) and truncated diffusion. SVS allocates varying diffusion steps according to lead time; shorter lead times are assigned fewer diffusion steps, while longer lead times linearly receive more steps. Truncated diffusion starts the reverse process at the intermediate state by utilizing deterministic result.

these issues, we replicate  $x^L$   $\hat{L}$  times to serve as the input for PB, which we denote as  $x^{\hat{L}}$ . Consequently, the forward process of PB, incorporating Eq. (3), is defined as follows.

$$x_t = (1 - m_t)x_0 + m_tx^{\hat{L}} + \sqrt{\delta_t}\epsilon, \quad (4)$$

$$x_{t-1} = (1 - m_{t-1})x_0 + m_{t-1}x^{\hat{L}} + \sqrt{\delta_{t-1}}\epsilon.$$

Here,  $m_t$  stands for a time weight, linearly increasing from 0 to 1 with respect to  $t$ . Concurrently,  $\delta_t$  denotes the variance defined as  $2(m_t - m_t^2)$ , and  $\epsilon$  corresponds to Gaussian noise, specifically  $N \sim (0, 1)$ . However, as  $x^{\hat{L}}$  consists of identical frames, spatial-temporal modeling is not feasible. To resolve this issue, we employ the feature  $z$  extracted from  $st(e(x))$  in the DB to perform cross-attention [28] as a condition in PB. Therefore, the object function of PB is as follows.

$$L_{PB} = \mathbb{E} \left\| m_t(x^{\hat{L}} - x_0) + \sqrt{\delta_t}\epsilon - \epsilon_{\theta}(x_t, t, z) \right\|^2. \quad (5)$$

The DB and PB are jointly trained in an end-to-end manner, and the total objective function for DGDM is defined as follows:

$$L_{\text{total}} = L_{PB} + L_{DB}. \quad (6)$$

**Sequential Variance Schedule** In weather forecasting, the uncertainty increases with the length of the lead time. To

Model	Diversity	#Param. (M)	#Flops (G)	Evaluate metric				
				MAE↓	MSE↓	PSNR↑	SSIM↑	FVD↓
ConvLSTM [32]	×	15.0M	56.79G	90.63	29.79	22.14	0.928	79.193
PredRNN [39]	×	23.8M	0.116T	72.82	23.96	23.28	0.946	50.407
PredRNN++ [38]	×	38.6M	0.172T	69.58	22.05	23.65	0.950	45.731
MIM [40]	×	38.0M	179.2G	70.67	22.92	23.53	0.948	47.530
PhyDNet [12]	×	3.1M	15.3G	61.47	20.35	24.21	0.955	38.752
SimVP [10]	×	58.0M	9.431G	89.04	32.14	21.83	0.926	72.969
TAU [34]	×	46.8M	15.953G	51.46	<b>15.68</b>	<b>25.71</b>	<b>0.966</b>	28.169
VDM [15]	✓	35.71M	77.446G	123.12	86.33	18.71	0.879	8.800
MCVD [37]	✓	28.0M	9.915G × 100	172.47	64.68	19.23	0.565	8.161
RaMViD [16]	✓	235.058M	1.052T × 1000	123.76	81.26	18.87	0.878	12.059
DGDM-DB	×	27.0M	11.456G	56.45	<u>17.88</u>	24.94	0.961	19.216
DGDM-SB	✓	63.3M	77.288G × 100	50.21	20.96	25.08	<u>0.962</u>	<u>7.461</u>
DGDM-Best	×	63.3M	77.288G × 100	<b>47.31</b>	19.14	<u>25.59</u>	<b>0.966</b>	<b>7.427</b>
DGDM-Average	✓	63.3M	(77.288G × 100) × 10	<u>48.54</u>	20.52	25.22	<b>0.966</b>	9.617

Table 1. Performance comparison results from the Moving MNIST dataset. For diffusion models, the amount of computation is indicated by the number of steps required in the reverse process. **Bold** indicates the best performance, and underline indicates the second-best performance.

capture this characteristic, we propose the sequential variance schedule (SVS). SVS is utilized during both the training and inference phases. Given the total number of diffusion steps  $T$  and the output length  $\hat{L}$ , the SVS for each lead time is defined by the equation:

$$\text{SVS} = \{T - (\hat{L} - i) \cdot S : i = 1, \dots, \hat{L}\} \quad (7)$$

Here,  $S$  denotes the step size of the diffusion steps.

### 3.3. Inference

To forecast the future weather condition  $y$ , the reverse process of the Brownian bridge starts at  $x_T = x^{\hat{L}}$ . Using the trained model, we then proceed through the reverse process that incrementally moves from  $x_t$  to  $x_{t-1}$ .

$$p_\theta(x_{t-1}|x_t) = N(x_{t-1}; \mu_\theta(x_t, t, z), \tilde{\delta}_t I), \quad (8)$$

where  $\mu_\theta(x_t, t, z)$  denotes the estimated mean value of the noise, and  $\tilde{\delta}_t$  is the variance of noise. We reach the ending point of the diffusion process, where  $x_0 = y$ . For acceleration, the inference process integrates a non-Markovian chain, as detailed in BBDM [22].

**Truncated Diffusion with Deterministic** By incorporating the results of DB  $\hat{y}$  into the reverse process, we can truncate the diffusion process, as illustrated in Figure 3. Specifically, substituting  $\hat{y}$  for  $x_0$  in Eq. (4) allows us to begin from an intermediate state,  $\hat{x}_t$ , rather than starting directly from the initial condition. The truncated reverse diffusion process of DGDM follows the equation:

$$\hat{x}_t = (1 - m_t)\hat{y} + m_t x_T + \sqrt{\delta_t}\epsilon. \quad (9)$$

Truncated diffusion not only modulates the diversity of results but also accelerates the speed of inference.

## 4. Experiments

In this section, we provide a comparative analysis using synthetic dataset and weather forecasting benchmarks to demonstrate the effectiveness of DGDM. Furthermore, we conduct comprehensive ablation studies to demonstrate the contributions of the components within our approach.

### 4.1. Experimental Setting

**Dataset** We use the Moving MNIST dataset, which is frequently used in future frame prediction tasks. Additionally, experiments are performed on two weather datasets: PNW-Typhoon and Weatherbench dataset. In our experiments, we train on the training set of each dataset and evaluate it on the test set.

- **Moving MNIST [33]** The Moving MNIST dataset contains 10,000 video sequences, each consisting of 20 frames. In each video sequence, two digits move independently around the frame, which has a spatial resolution of  $64 \times 64$  pixels. The digits frequently intersect with each other and bounce off the edges of the frame. Consequently, the values of  $C, L, \hat{L}, H, W$  are 1, 10, 10, 64, and 64 respectively.
- **PNW-Typhoon** The Pacific Northwest Windstorm (PNW)-Typhoon weather satellite dataset is a collection that records typhoons observed from January 2019 to September 2023. The PNW-Typhoon dataset is sourced from the GK2A (GEO-KOMPSAT-2A) satellite. PNW-Typhoon dataset used observations at 1-hour intervals over the East Asia regions with a 2 km spatial resolution. All data preprocessing strictly adhered to the official GK2A user manual<sup>2</sup> to maintain the integrity of the GK2A physical value data. The image dimensions in the GK2A dataset are  $128 \times 128$ . In our experiments, we exclusively use channels of the infrared ray (IR) at  $10.5 \mu\text{m}$ ,

<sup>2</sup><https://nmsc.kma.go.kr/enhome/html/base/cmm/selectPage.do?page=satellite.gk2a.intro>

Model	PNW-Typhoon														
	MSE ↓			MAE ↓			PSNR ↑			SSIM ↑			FVD ↓		
	IR	SW	WV	IR	SW	WV	IR	SW	WV	IR	SW	WV	IR	SW	WV
ConvLSTM [32]	937.80	1075.43	409.65	2973.50	3221.82	1952.39	13.06	14.31	17.94	0.399	0.400	0.642	1689.39	1321.36	993.59
PredRNN [39]	774.73	804.28	253.28	2342.76	2933.85	1756.32	14.23	14.57	18.34	0.401	0.403	0.629	1640.11	1293.09	1033.27
PredRNN++ [38]	667.18	739.01	213.51	2372.64	3088.18	1552.26	13.51	14.55	20.29	0.414	0.410	0.630	1340.61	1040.10	926.51
MIM [40]	625.99	683.51	195.14	2398.68	3127.97	1567.28	13.85	13.95	17.55	0.392	0.392	0.613	1262.59	969.19	954.53
PhyDNet [12]	655.14	728.93	189.02	2460.73	3144.94	1675.00	14.42	14.10	18.96	0.408	0.398	0.576	1305.54	1007.79	944.65
SimVP [10]	643.06	706.72	204.33	2452.73	3079.17	1609.57	14.01	14.21	19.17	0.401	0.406	0.598	1283.45	991.53	940.42
TAU [34]	565.47	664.50	166.11	2117.84	2842.39	1493.33	15.12	14.82	19.49	0.404	0.418	0.603	997.47	880.41	891.90
VDM [15]	881.08	1128.37	401.52	2794.82	3355.41	2063.66	13.43	12.31	17.07	0.371	0.383	0.607	830.29	727.09	573.47
MCVD [37]	605.51	904.93	472.19	2166.98	2799.92	2300.42	14.89	13.57	16.74	0.430	0.433	0.647	737.99	439.97	481.70
RaMViD [16]	770.72	1152.08	341.68	2781.69	3355.09	1803.71	13.96	12.55	18.39	0.392	0.392	0.624	1091.97	935.57	<b>395.73</b>
DGDM-DB	495.52	576.78	133.16	1949.46	2162.01	1031.67	15.89	15.43	21.785	0.442	0.436	0.653	819.72	710.32	799.30
DGDM-SB	461.90	540.79	121.27	1875.08	2065.37	1003.18	16.08	15.57	21.910	0.478	0.457	0.678	<u>705.56</u>	<u>422.03</u>	508.36
DGDM-Best	<u>459.85</u>	<u>533.35</u>	<u>120.75</u>	<u>1871.08</u>	<u>2047.80</u>	<u>1000.82</u>	<u>16.10</u>	<u>15.63</u>	<u>21.932</u>	<u>0.480</u>	<u>0.460</u>	<u>0.679</u>	<b>698.93</b>	<b>414.07</b>	<u>502.26</u>
DGDM-Average	<b>456.11</b>	<b>516.66</b>	<b>120.34</b>	<b>1863.26</b>	<b>2004.71</b>	<b>998.31</b>	<b>16.15</b>	<b>15.83</b>	<b>21.955</b>	<b>0.482</b>	<b>0.483</b>	<b>0.682</b>	733.03	482.80	531.14

Table 2. Performance comparison results from the PNW-Typhoon dataset. IR stands for infrared red, WV stands for water vapor, and SW stands for short wave, representing each channel of the weather observation satellite.

short wave infrared ray (SW) at  $0.38 \mu\text{m}$ , and water vapor (WV) at  $0.69 \mu\text{m}$ . Typhoons from 2019 to 2022 are used for training, while the ones from 2023 are used for testing. Consequently, the values for  $C, L, \hat{L}, H, W$  are 3, 10, 10, 128, and 128, respectively.

- **Weatherbench [26]** The WeatherBench dataset is a comprehensive weather forecasting collection that encompasses various climatic factors. The raw data is re-gridded to a  $5.625^\circ$  resolution, equivalent to a  $32 \times 64$  grid. We employ the WeatherBench-S framework from [35], where each climatic factor is trained individually. The model is trained using data spanning 2010 to 2015, validated using data from 2016, and tested with 2017-2018 data, maintaining a temporal granularity of one hour. Consequently, the values for  $C, L, \hat{L}, H, W$  are 1, 12, 12, 32, and 64, respectively.

**Evaluation Metric** For evaluating DGDM, we use mean squared error (MSE) to heavily penalize larger errors and mean absolute error (MAE) for a linear error penalty. We utilize peak signal-to-noise ratio (PSNR) to evaluate the quality of signal representation against corrupting noise, and structural similarity index measure (SSIM) [41] to assess perceptual results. Additionally, we employ Fréchet video distance (FVD) to measure the similarity between the generated videos and the ground truth videos in feature space.

**Implementation Details** For our implementation, the Adam optimizer is employed with a learning rate of  $1e^{-4}$  for the diffusion model and  $3e^{-4}$  for the deterministic model. We train with a mini-batch size of 8. The learning rate is adaptively adjusted using the ReduceLROnPlateau scheduler. We adopt a forwarding process of 1,000 steps and a reverse process of 200 steps. However, the reverse process is truncated after 100 steps. To enhance model sta-

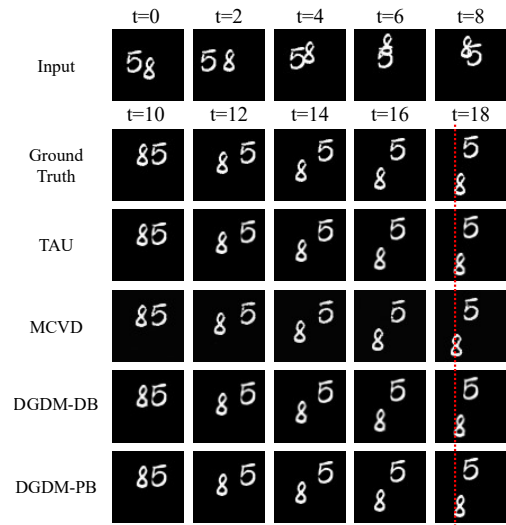


Figure 4. Visualization of Moving MNIST with time stride of 2.

bility, we implement exponential moving average (EMA) with a decay factor of 0.995. The number of training epochs varies by dataset: 2,000 for the Moving MNIST, 200 for the PNW-typhoon dataset, and 50 for the WeatherBench dataset. All experiments are conducted using the PyTorch framework on a single A100 GPU. Detailed network architectures are provided in the supplementary material.

## 4.2. Experimental Results

**Moving MNIST** We evaluate DGDM on the Moving MNIST dataset to verify its effectiveness in the video frame prediction task. We compare the performance with existing data-driven video frame prediction models [10, 12, 32, 34, 38–40] on the Moving MNIST dataset. As shown in Table 1, models without diversity all achieve better scores in MAE, MSE, PSNR, and SSIM, but exhibit low FVD. This

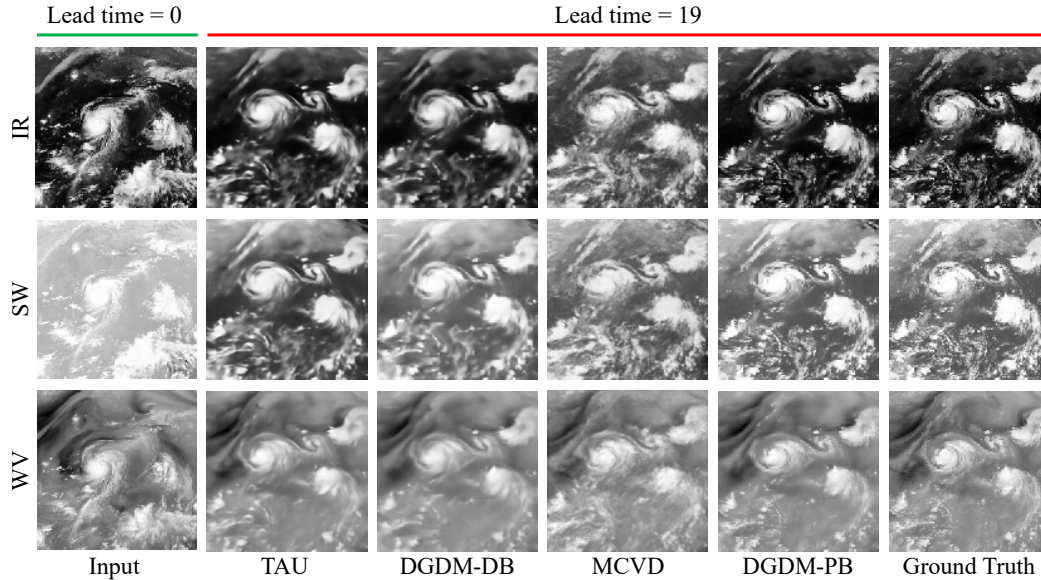


Figure 5. Qualitative comparison results on the PWN-Typhoon dataset. TAU [34] and MCVD [37] are the best-performing approaches in deterministic and probabilistic models, respectively.

suggests that while deterministic models are adept at predicting future movements in the Moving MNIST dataset, they struggle to replicate finer details, such as texture. In contrast, video generation models with diversity score competitively on FVD yet have significantly worse MAE, MSE, PSNR, and SSIM compared to deterministic models. As illustrated in Figure 4, these experimental analyses offer insights that corroborate our observations: deterministic models precisely predict locations but lack the clarity of the GT, whereas probabilistic models, despite their clarity, do not predict locations as accurately. However, the DGDM demonstrates a close resemblance to the GT in both location accuracy and clarity.

Despite the existence of diversity, DGDM is able to obtain state-of-the-art results for all MAE, SSIM, and FVD. These experimental results show that DGDM is a model that is as accurate as we intended but produces diverse results. Furthermore, our model possesses diversity, making ensemble methods possible. When ensemble techniques are employed, DGDM achieves better scores in MAE, MSE, PSNR, and SSIM. However, despite these achievements, performance with respect to FVD declined in random selection. The same averaging might result in outputs that, while closer to the GT in a pixel-wise sense, might lack some of the higher-level semantic nuances or temporal coherence.

**PNW-Typhoon** Table 2 shows the results of verifying video frame prediction methods and video generation methods on the PNW-Typhoon dataset. The experimental results in Table 2 show that, unlike the experimental results in Ta-

Model	WeatherBench					
	Temperature (t2m)		Humidity (r)		Wind (uv10)	
	MSE	RMSE	MSE	RMSE	MSE	RMSE
ConvLSTM [32]	1.521	1.233	35.146	5.928	1.8976	1.3775
PredRNN [39]	1.331	1.154	37.611	6.133	1.8810	1.3715
PredRNN++ [38]	1.634	1.278	35.146	5.928	1.8727	1.3685
MIM [40]	1.784	1.336	36.534	6.044	3.1399	1.7720
SimVP [10]	1.238	1.113	34.355	5.861	1.9993	1.4140
TAU [34]	<b>1.162</b>	<b>1.078</b>	31.831	5.642	<b>1.5925</b>	<b>1.2619</b>
VDM [15]	2.343	1.530	43.293	6.579	2.2345	1.4948
MCVD [37]	2.512	1.584	45.691	6.759	2.2213	1.4904
RaMViD [16]	1.908	1.381	39.028	6.247	2.7639	1.6624
DGDM-Best	<b>1.025</b>	<b>1.012</b>	<b>28.572</b>	<b>5.345</b>	<b>1.5914</b>	<b>1.2615</b>
DGDM-Average	1.183	1.087	<b>30.326</b>	<b>5.506</b>	1.6439	1.2821

Table 3. Quantitative comparison results between DGDM and other baselines on the WeatherBench dataset.

ble 1, most of the deterministic models perform poorly in MSE and MAE compared to probabilistic models. These experimental results show that probabilistic models have potential in the field of high-resolution regional weather forecasting.

Figure 5 presents a qualitative analysis of deterministic and probabilistic models, specifically, TAU and MCVD. In typhoon analysis, aspects like the eye of the typhoon, its size, and the way clouds disperse and coalesce are critical. As depicted in Figure 5, while the deterministic models simulate the size of the typhoon well, the results are too blurry to definitively assess the eye of the typhoon or the cloud patterns. On the other hand, MCVD provides clearer images but falls short in predicting the size of the typhoon and cloud formation. DGDM, a probabilistic model, most accurately

Components					Deterministic		Probabilistic	
DB	PB	BB	LF	SVS	MAE	FVD	MAE	FVD
✓					58.13	18.50	-	-
	✓				-	-	123.20	8.80
✓	✓				95.09	58.83	110.07	14.74
	✓	✓			-	-	89.45	17.05
✓	✓	✓			56.71	20.51	52.04	10.06
✓	✓	✓	✓		56.18	18.72	50.35	9.31
✓	✓	✓	✓	✓	56.45	19.22	<b>50.22</b>	<b>8.28</b>

Table 4. Quantitative comparisons on components of DGDM.

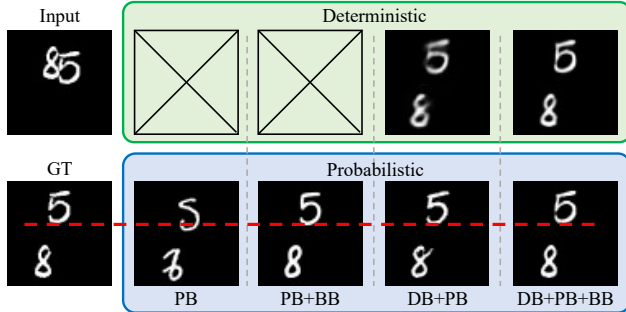


Figure 6. Visualization the results by components. For illustration purposes, we use the same data as in Figure 4.

simulates the size of a typhoon and is also the most precise in predicting the formation and dissipation of clouds. These experimental results suggest that DGDM is highly effective for high-resolution regional weather forecasting.

**WeatherBench** Table 3 shows the results of quantitative experiments in WeatherBench, a global weather forecasting dataset. DGDM-Best, a method of selecting the sample with the highest performance among all 20 samples, achieves the best performance in the WeatherBench dataset. In addition, DGDM-Average, which ensembles all 20 models, shows the second-best performance in the Humidity modality. These experimental results indicate that DGDM has high usability even if a single output is not selected and simply ensemble with average.

### 4.3. Ablation Study

We perform ablation studies on the Moving MNIST dataset to evaluate the effects of the components and the initial point.

**Effect of Each Component** As shown in Table 4 and Figure 6, using only the results of PB in clear images that, however, differ from the GT. Moreover, when PB is combined with the BB, the resulting images are more closely aligned with the actual GT, as opposed to those produced by PB alone. Lastly, the DB, the replication of the last frame (LF), and the SVS all contribute to improvements in MAE and

Diffusion steps	Evaluate metric						
	MSE		MAE		FVD		
	Mean	STD	Mean	STD	Mean	STD	
w/o truncated	200	23.621	0.105	51.223	0.126	8.282	0.087
	175	23.326	0.066	50.561	0.079	8.600	0.121
	150	23.146	0.066	50.363	0.083	8.221	0.149
	125	23.453	0.145	51.340	0.190	8.487	0.122
	100	23.222	0.058	52.046	0.081	8.132	0.154
w/ truncated	175	21.947	0.046	49.543	0.080	8.326	0.079
	150	21.613	0.031	<b>49.498</b>	0.052	8.126	0.080
	125	21.370	0.028	49.792	0.034	7.913	0.072
	100	<b>20.963</b>	0.021	50.210	0.033	<b>7.461</b>	0.068

Table 5. Quantitative results with different diffusion steps.

FVD performance. These experimental results demonstrate that all components of DGDM are complementary to each other. Interestingly, it has been observed that when DB and PB are trained together, the performance of DB also improves. This outcome indicates that the DGDM pipeline is effective not only for PB but also for DB. Particularly noteworthy is that SVS enhances MAE and FVD performance and also accelerates inference speed for frames with shorter lead times. While the total diffusion steps may be the same as those in diffusion models without SVS, SVS completes inference earlier for frames with shorter lead times due to fewer diffusion steps being required.

**Effect of Truncated Diffusion with Deterministic** Table 5 shows the results of the reverse process based on the denoising steps. When using a non-Markovian chain without truncated diffusion, there appears to be no significant relationship between the number of diffusion steps and MAE, MSE, and FVD. On the other hand, setting the reverse step to 200 and using deterministic results to truncate the reverse process to reduce the diffusion step significantly improves accuracy. In addition, a trend is apparent where reducing diffusion steps leads to a lower standard deviation (STD) of MAE, MSE and FVD. This suggests that our method can effectively modulate uncertainty in weather forecasting. In addition, truncated diffusion improves computational efficiency without degrading performance.

## 5. Conclusion

In this paper, we introduce the Deterministic Guidance Diffusion Model for Probabilistic Weather Forecasting (DGDM). DGDM bridges the gap between the accuracy of deterministic models and the diversity of probabilistic models, addressing the limitations of existing data-driven models that face a trade-off between probabilistic forecasting and accuracy. To validate DGDM in high-resolution weather forecasting, we introduce the Pacific Northwest Windstorm (PNW)-Typhoon weather satellite dataset. We evaluate DGDM using the Moving MNIST, PNW-Typhoon,

and WeatherBench datasets, and it achieves state-of-the-art results in most of the evaluated metrics. We envision DGDM becoming a cornerstone in the domain of weather forecasting.

**Limitations and Future work** Due to its utilization of deterministic guidance, DGDM can generate samples that are both closely aligned with the future weather conditions and diverse. However, a challenge persists for DGDM, as it is fundamentally a probabilistic model. This necessitates the careful selection of a sample from various possibilities to closely match future weather conditions. We will study methods for selecting the best sample from a variety of possibilities, rather than simply average ensembling.

## References

- [1] Georgy Ayzel, Tobias Scheffer, and Maik Heistermann. Rainnetv1.0: a convolutional neural network for radar-based precipitation nowcasting. *Geoscientific Model Development*, 13(6):2631–2644, 2020. [2](#)
- [2] Mohammad Babaeizadeh, Chelsea Finn, Dumitru Erhan, Roy H Campbell, and Sergey Levine. Stochastic variational video prediction. *arXiv preprint arXiv:1710.11252*, 2017. [3](#)
- [3] Kaifeng Bi, Lingxi Xie, Hengheng Zhang, Xin Chen, Xiaotao Gu, and Qi Tian. Accurate medium-range global weather forecasting with 3d neural networks. *Nature*, 619(7970):533–538, 2023. [2](#)
- [4] Guy P. Brasseur and Daniel J. Jacob. *Parameterization of Subgrid-Scale Processes*, page 342–398. Cambridge University Press, 2017. [2](#)
- [5] Andrew Brown, Sean Milton, Mike Cullen, Brian Golding, John Mitchell, and Ann Shelly. Unified modeling and prediction of weather and climate: A 25-year journey. *Bulletin of the American Meteorological Society*, 93(12):1865–1877, 2012. [1](#)
- [6] Joel Janek Dabrowski, Yifan Zhang, and Ashfaqur Rahman. Forecastnet: a time-variant deep feed-forward neural network architecture for multi-step-ahead time-series forecasting. In *NeurIPS*, pages 579–591. Springer, 2020. [2](#)
- [7] Dick P Dee, S M Uppala, Adrian J Simmons, Paul Berrisford, Paul Poli, Shinya Kobayashi, U Andrae, MA Balmaseda, G Balsamo, d P Bauer, et al. The era-interim reanalysis: Configuration and performance of the data assimilation system. *Quarterly Journal of the royal meteorological society*, 137(656):553–597, 2011. [1](#)
- [8] Piotr Dollr, Christian Wojek, Bernt Schiele, and Pietro Perona. Pedestrian detection: A benchmark. In *CVPR*, pages 304–311, 2009. [2](#)
- [9] Zhihan Gao, Xingjian Shi, Boran Han, Hao Wang, Xiaoyong Jin, Danielle Maddix, Yi Zhu, Mu Li, and Yuyang Wang. Prediff: Precipitation nowcasting with latent diffusion models. *arXiv preprint arXiv:2307.10422*, 2023. [2](#)
- [10] Zhangyang Gao, Cheng Tan, Lirong Wu, and Stan Z. Li. Simvp: Simpler yet better video prediction. In *CVPR*, pages 3170–3180, 2022. [3](#), [5](#), [6](#), [7](#)
- [11] Aleksandra Gruca, Federico Serva, Lloren Lliso, Pilar Ripodas, Xavier Calbet, Pedro Herruzo, Ji Pihrt, Rudolf Raevskiy, Petr Simanek, Matej Choma, et al. Weather4cast at neurips 2022: Super-resolution rain movie prediction under spatio-temporal shifts. In *NeurIPS 2022 Competition Track*, pages 292–313. PMLR, 2022. [2](#)
- [12] Vincent Le Guen and Nicolas Thome. Disentangling physical dynamics from unknown factors for unsupervised video prediction. In *CVPR*, pages 11474–11484, 2020. [2](#), [5](#), [6](#)
- [13] Dan Hendrycks and Kevin Gimpel. Gaussian error linear units (gelus). *arXiv preprint arXiv:1606.08415*, 2016. [2](#), [3](#)
- [14] Jonathan Ho, Ajay Jain, and Pieter Abbeel. Denoising diffusion probabilistic models. *NeurIPS*, 33:6840–6851, 2020. [3](#)
- [15] Jonathan Ho, Tim Salimans, Alexey Gritsenko, William Chan, Mohammad Norouzi, and David J Fleet. Video diffusion models. *arXiv:2204.03458*, 2022. [3](#), [4](#), [5](#), [6](#), [7](#)
- [16] Tobias Höppe, Arash Mehrjou, Stefan Bauer, Didrik Nielsen, and Andrea Dittadi. Diffusion models for video prediction and infilling. *Transactions on Machine Learning Research*, 2022. [3](#), [5](#), [6](#), [7](#)
- [17] Xiaotao Hu, Zhewei Huang, Ailin Huang, Jun Xu, and Shuchang Zhou. A dynamic multi-scale voxel flow network for video prediction. In *CVPR*, pages 6121–6131, 2023. [3](#)
- [18] Catalin Ionescu, Dragos Papava, Vlad Olaru, and Cristian Sminchisescu. Human3.6m: Large scale datasets and predictive methods for 3d human sensing in natural environments. *IEEE TPAMI*, 36(7):1325–1339, 2013. [2](#)
- [19] JP Iorio, PB Duffy, B Govindasamy, SL Thompson, M Khairoutdinov, and D Randall. Effects of model resolution and subgrid-scale physics on the simulation of precipitation in the continental united states. *Climate Dynamics*, 23:243–258, 2004. [1](#)
- [20] Remi Lam, Alvaro Sanchez-Gonzalez, Matthew Willson, Peter Wirnsberger, Meire Fortunato, Alexander Pritzel, Suman Ravuri, Timo Ewalds, Ferran Alet, Zach Eaton-Rosen, et al. Graphcast: Learning skillful medium-range global weather forecasting. *arXiv preprint arXiv:2212.12794*, 2022. [2](#)
- [21] Jussi Leinonen, Ulrich Hamann, Daniele Nerini, Urs Germann, and Gabriele Franch. Latent diffusion models for generative precipitation nowcasting with accurate uncertainty quantification. *arXiv preprint arXiv:2304.12891*, 2023. [2](#)
- [22] Bo Li, Kaitao Xue, Bin Liu, and Yu-Kun Lai. Bbdm: Image-to-image translation with brownian bridge diffusion models. In *CVPR*, pages 1952–1961, 2023. [4](#), [5](#)
- [23] Pauline Luc, Aidan Clark, Sander Dieleman, Diego de Las Casas, Yotam Doron, Albin Cassirer, and Karen Simonyan. Transformation-based adversarial video prediction on large-scale data. *arXiv preprint arXiv:2003.04035*, 2020. [3](#)
- [24] Shuliang Ning, Mengcheng Lan, Yanran Li, Chaofeng Chen, Qian Chen, Xunlai Chen, Xiaoguang Han, and Shuguang Cui. Mimo is all you need: a strong multi-in-multi-out baseline for video prediction. In *AAAI*, volume 37, pages 1975–1983, 2023. [3](#)
- [25] Ruslan Rakhimov, Denis Volkhonskiy, Alexey Artemov, Denis Zorin, and Evgeny Burnaev. Latent video transformer. *arXiv preprint arXiv:2006.10704*, 2020. [3](#)
- [26] Stephan Rasp, Peter D Dueben, Sebastian Scher, Jonathan A Weyn, Soukayna Mouatadid, and Nils Thuerey. Weatherbench: a benchmark data set for data-driven weather forecasting. *Journal of Advances in Modeling Earth Systems*, 12(11):e2020MS002203, 2020. [6](#)
- [27] Suman Ravuri, Karel Lenc, Matthew Willson, Dmitry Kangin, Remi Lam, Piotr Mirowski, Megan Fitzsimons, Maria Athanassiadou, Sheleem Kashem, Sam Madge, et al. Skillful precipitation nowcasting using deep generative models of radar. *Nature*, 597(7878):672–677, 2021. [2](#)
- [28] Robin Rombach, Andreas Blattmann, Dominik Lorenz, Patrick Esser, and Bjorn Ommer. High-resolution image synthesis with latent diffusion models. In *CVPR*, pages 10684–10695, 2022. [4](#)
- [29] Minseok Seo, Doyi Kim, Seungheon Shin, Eunbin Kim, Sewoong Ahn, and Yeji Choi. Simple baseline for weather forecasting using spatiotemporal context aggregation network. *arXiv preprint arXiv:2212.02952*, 2022. [2](#)
- [30] Minseok Seo, Hakjin Lee, Doyi Kim, and Junghoon Seo. Implicit stacked autoregressive model for video prediction. *arXiv preprint arXiv:2303.07849*, 2023. [3](#), [1](#)

- [31] Wenzhe Shi, Jose Caballero, Ferenc Huszár, Johannes Totz, Andrew P Aitken, Rob Bishop, Daniel Rueckert, and Zehan Wang. Real-time single image and video super-resolution using an efficient sub-pixel convolutional neural network. In *CVPR*, pages 1874–1883, 2016. [2](#)
- [32] Xingjian Shi, Zhourong Chen, Hao Wang, Dit-Yan Yeung, Wai-Kin Wong, and Wang-chun Woo. Convolutional lstm network: A machine learning approach for precipitation nowcasting. *NeurIPS*, 28, 2015. [2](#), [5](#), [6](#), [7](#)
- [33] Nitish Srivastava, Elman Mansimov, and Ruslan Salakhudinov. Unsupervised learning of video representations using lstms. In *International conference on machine learning*, pages 843–852. PMLR, 2015. [5](#)
- [34] Cheng Tan, Zhangyang Gao, Lirong Wu, Yongjie Xu, Jun Xia, Siyuan Li, and Stan Z Li. Temporal attention unit: Towards efficient spatiotemporal predictive learning. In *CVPR*, pages 18770–18782, 2023. [3](#), [5](#), [6](#), [7](#), [1](#)
- [35] Cheng Tan, Siyuan Li, Zhangyang Gao, Wenfei Guan, Zedong Wang, Zicheng Liu, Lirong Wu, and Stan Z Li. Openstl: A comprehensive benchmark of spatio-temporal predictive learning. In *Conference on Neural Information Processing Systems Datasets and Benchmarks Track*, 2023. [6](#)
- [36] Kevin Trebing, Tomasz Stanczyk, and Siamak Mehrkanoon. Smaat-unet: Precipitation nowcasting using a small attention-unet architecture. *Pattern Recognition Letters*, 145:178–186, 2021. [2](#)
- [37] Vikram Voleti, Alexia Jolicoeur-Martineau, and Chris Pal. Mcvd-masked conditional video diffusion for prediction, generation, and interpolation. *NeurIPS*, 35:23371–23385, 2022. [3](#), [5](#), [6](#), [7](#)
- [38] Yunbo Wang, Zhifeng Gao, Mingsheng Long, Jianmin Wang, and S Yu Philip. Predrnn++: Towards a resolution of the deep-in-time dilemma in spatiotemporal predictive learning. In *International Conference on Machine Learning*, pages 5123–5132. PMLR, 2018. [2](#), [5](#), [6](#), [7](#)
- [39] Yunbo Wang, Mingsheng Long, Jianmin Wang, Zhifeng Gao, and Philip S Yu. Predrnn: Recurrent neural networks for predictive learning using spatiotemporal lstms. *NeurIPS*, 30, 2017. [2](#), [5](#), [6](#), [7](#)
- [40] Yunbo Wang, Jianjin Zhang, Hongyu Zhu, Mingsheng Long, Jianmin Wang, and Philip S Yu. Memory in memory: A predictive neural network for learning higher-order non-stationarity from spatiotemporal dynamics. In *CVPR*, pages 9154–9162, 2019. [5](#), [6](#), [7](#)
- [41] Zhou Wang, Alan C Bovik, Hamid R Sheikh, and Eero P Simoncelli. Image quality assessment: from error visibility to structural similarity. *IEEE TIP*, 13(4):600–612, 2004. [6](#)
- [42] Junbo Zhang, Yu Zheng, and Dekang Qi. Deep spatiotemporal residual networks for citywide crowd flows prediction. In *AAAI*, volume 31, 2017. [2](#)
- [43] Yiqi Zhong, Luming Liang, Ilya Zharkov, and Ulrich Neumann. Mmvp: Motion-matrix-based video prediction. In *ICCV*, pages 4273–4283, 2023. [3](#)

# Deterministic Guidance Diffusion Model for Probabilistic Weather Forecasting

## Supplementary Material

### A. Introduction

In this supplementary material we provide additional information as follows:

- Architecture details of DGDM.
- Additional qualitative results.

### B. Implementation Details

In this section, we provide implementation details of the Deterministic Guidance Diffusion Model (DGDM). Table 6 shows the hyperparameter settings used in all of our experiments with DGDM. Please note that while the number of training epochs differ depending on the training dataset (Moving MNIST: 2000, PNW-Typhoon: 200, WeatherBench: 50), the hyperparameters remain constant across all datasets.

Hyperparameter	Value
Optimizer	Adam
Learning rate of DB	$1e^{-3}$
Learning rate of PB	$1e^{-4}$
$\beta_1$	0.9
$\beta_2$	0.999
Weight decay	0.0
Learning rate scheduler	ReduceLROnPlateau
Min learning rate	$5e^{-6}$
Factor	0.5
Patience	3,000
Cool down	3,000
Threshold	$1e^{-4}$
EMA decay	0.995
EMA Start step	30,000
EMA update interval	8

Table 6. DGDM training settings. Note that all hyperparameters are applied equally to all datasets.

In addition, we present the detailed architecture of the deterministic and probability branches of the DGDM. As shown in Table 7, the Deterministic branch adopts an encoder-translator-decoder structure, a leading approach in recent deterministic video frame prediction [30, 34]. Table 8 presents the architecture details of the probability branch. The probability branch of DGDM employs a 3D-UNet architecture, which is identical to that used in video diffusion models.

### C. Additional Qualitative Results

In this section, we provide additional qualitative results that could not be included in the main text. Figure 7 shows the qualitative analysis of DGDM-Best (20 samples) from the PNW-Typhoon dataset. As seen in the figure, DGDM-Deterministic shows blurry results, but DGDM-Probability yields relatively clear results. These qualitative experimental results demonstrate that DGDM can be useful not only in predicting large-scale climate phenomena but also smaller-scale ones.

Figure 8 shows the qualitative experimental results of DGDM in the WeatherBench dataset. As can be seen in the figure, DGDM demonstrates its effectiveness in global climate modeling, such as with WeatherBench.

Block	Layer	Resolution	Channels
<b>Encoder</b>			
2D CNN	Conv3×3	$H \times W$	$C \rightarrow 64$
	LayerNorm		64
	SiLU		64
2D CNN	Conv3×3	$H \times W \rightarrow H/2 \times W/2$	64
	LayerNorm		64
	SiLU		64
2D CNN	Conv3×3	$H/2 \times W/2$	64
	LayerNorm		64
	SiLU		64
2D CNN	Conv3×3	$H/2 \times W/2 \rightarrow H/4 \times W/4$	64
	LayerNorm		64
	SiLU		64
<b>Translator</b>			
ConvNext×8	Conv7×7	$H/4 \times W/4$	$64 \rightarrow 64 \times T$
	LayerNorm		$64 \times T$
	Linear		$64 \times T \rightarrow 256 \times T$
	GELU		$256 \times T$
	Linear		$256 \times T \rightarrow 64 \times T$
<b>Decoder</b>			
2D CNN	Conv3×3	$H/4 \times W/4$	$64 \times T \rightarrow 64$
	LayerNorm		$64 \rightarrow 256$
	SiLU		256
Upsample	Pixelshuffle	$H/4 \times W/4 \rightarrow H/2 \times W/2$	256 → 64
2D CNN	Conv3×3	$H/2 \times W/2$	64
	LayerNorm		64
	SiLU		64
2D CNN	Conv3×3	$H/2 \times W/2$	$64 \rightarrow 256$
	LayerNorm		256
	SiLU		256
Upsample	Pixelshuffle	$H/2 \times W/2 \rightarrow H \times W$	256 → 64
2D CNN	Conv3×3	$H \times W$	$64 \rightarrow 64$
	LayerNorm		64
	SiLU		64
Readout	Reshape	$H \times W$	$64 \rightarrow 64 \times T$
	Conv3×3		$64 \times T \rightarrow C \times T$

Table 7. Detailed architecture of the deterministic branch. **Conv3x3** denotes a 2D convolution layer with a 3×3 kernel size, while **LayerNorm** refers to layer normalization. **SiLU** is the Sigmoid Linear Unit activation layer [13], and **Pixelshuffle** is a upsampling layer [31] that rearrange channel dimension into the spatial dimension. Throughout the encoder and decoder, the time dimension  $T$  is treated as a batch, while in the Translator and the final convolutional layer, it is reshaped into the channel dimension.

Block	Layer	Resolution	Channels
Initial Block	Conv7×7	$H \times W$	$C \rightarrow 64$
	TeAttention		64
Time MLP	Linear		$64 \rightarrow 256$
	GELU		256
	Linear		256
Cond Block	Conv3×3	$H/4 \times W/4$	64
	GroupNorm8		64
	SiLU		64
	Conv3×3	$H/4 \times W/4$	64
	GroupNorm8		64
	SiLU		64
Down Block	ResBlock	$H \times W$	64
	ResBlock	$H \times W$	64
	SpAttention		64
	TeAttention		64
	Conv4×4	$H \times W \rightarrow H/2 \times W/2$	64
Down Block	ResBlock	$H/2 \times W/2$	$64 \rightarrow 128$
	ResBlock	$H/2 \times W/2$	128
	SpAttention		128
	TeAttention		128
	Conv4×4	$H/2 \times W/2 \rightarrow H/4 \times W/4$	128
Down Block	ResBlock	$H/4 \times W/4$	$128 \rightarrow 256$
	ResBlock	$H/4 \times W/4$	256
	SpAttention		256
	TeAttention		256
	Conv4×4	$H/4 \times W/4 \rightarrow H/8 \times W/8$	256
Down Block	ResBlock	$H/8 \times W/8$	$256 \rightarrow 512$
	ResBlock	$H/8 \times W/8$	512
	SpAttention		512
	TeAttention		512
Mid Block	ResBlock	$H/8 \times W/8$	512
	SpAttention		512
	TeAttention		512
	ResBlock	$H/8 \times W/8$	512
Up Block	ResBlock	$H/8 \times W/8$	$1024 \rightarrow 256$
	ResBlock	$H/8 \times W/8$	256
	SpAttention		256
	TeAttention		256
	Deconv4×4	$H/8 \times W/8 \rightarrow H/4 \times W/4$	256
Up Block	ResBlock	$H/4 \times W/4$	$512 \rightarrow 128$
	ResBlock	$H/4 \times W/4$	128
	SpAttention		128
	TeAttention		128
	Deconv4×4	$H/4 \times W/4 \rightarrow H/2 \times W/2$	128
Up Block	ResBlock	$H/2 \times W/2$	$256 \rightarrow 64$
	ResBlock	$H/2 \times W/2$	64
	PoAttention		64
	TeAttention		64
	Deconv4×4	$H/2 \times W/2 \rightarrow H \times W$	64
Up Block	ResBlock	$H \times W$	$128 \rightarrow 64$
	ResBlock	$H \times W$	64
	SpAttention		64
	TeAttention		64
Out Block	ResBlock	$H \times W$	$192 \rightarrow 64$
	Conv1×1	$H \times W$	$64 \rightarrow C$

Table 8. Detailed architecture of the probabilistic branch. **Conv7×7**, **Conv3×3**, and **Conv1×1** are 3D convolutional layers with kernel sizes of  $1 \times 7 \times 7$ ,  $1 \times 3 \times 3$ , and  $1 \times 1 \times 1$ , respectively. **GroupNorm8** is the Group Normalization layer with 8 groups. **Time MLP** is the block used for embed the denoising step  $t$ . **SiLU** and **GeLU** are the Sigmoid Linear Unit and Gaussian Error Linear Unit activation layers [13], respectively. **ResNetBlock** consists of a sequence with a Linear layer addressing the denoising step  $t$  followed by a SiLU activation, two blocks of Conv3×3, GroupNorm8, and SiLU activation. **SpAttention** is a spatial attention layer that considers only the spatial dimension with deterministic features. **TeAttention** is a self-attention layer that focuses on the temporal dimension of sequential data. Downsampling is performed by **Conv4×4**, a 3D convolutional layer with a stride of 2 and a  $1 \times 4 \times 4$  kernel size and upsampling is performed through **Deconv4×4**, a 3D transposed convolutional layer with the same stride and kernel size. **Up block** receives concatenated inputs from the features of previous block and the features of down block, which have the same resolution. The **Out block** also use skip connection and further concatenates deterministic features for input.

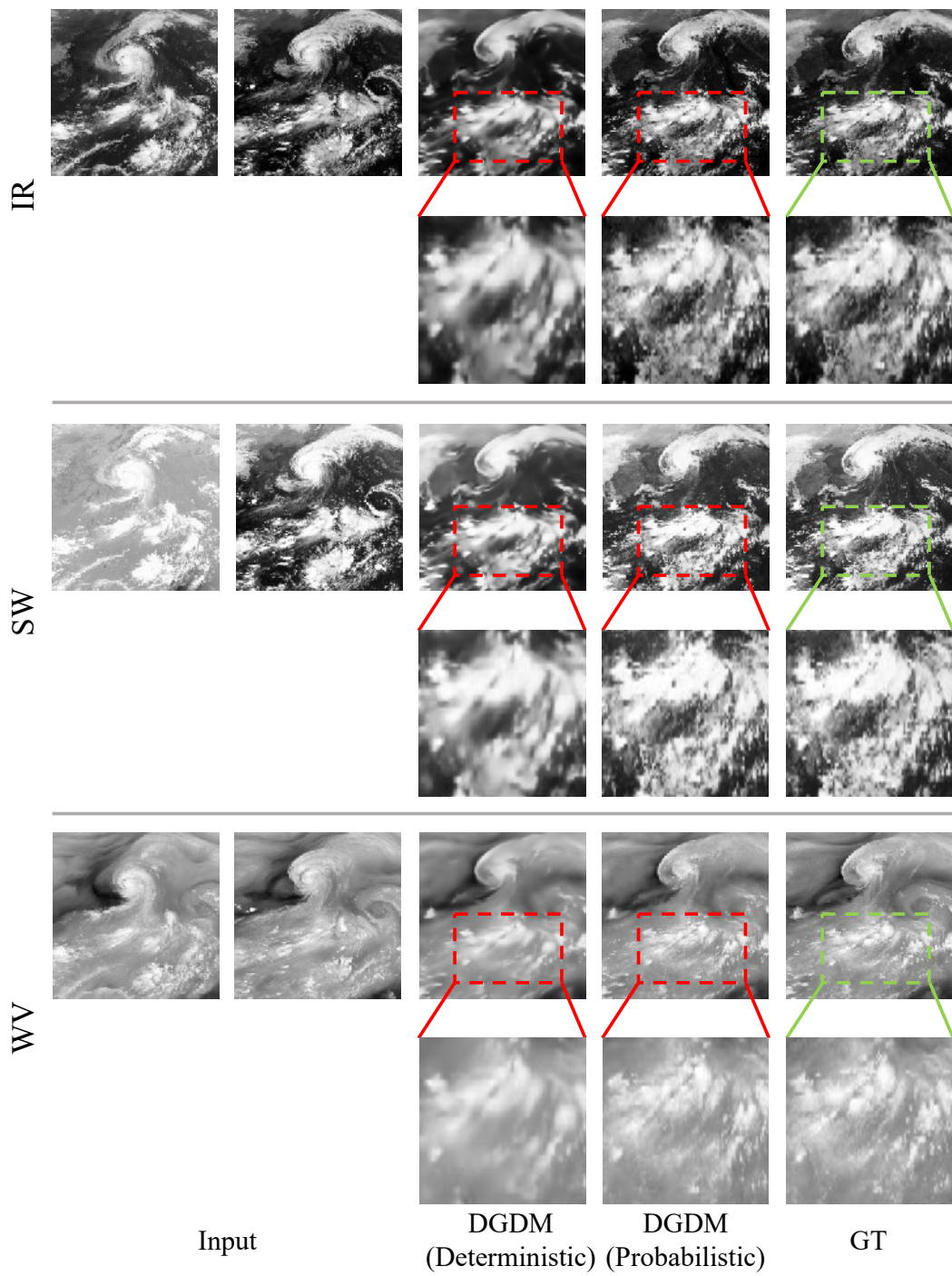


Figure 7. Qualitative experimental results from the PNW-Typhoon dataset with DGDM. The two samples on the left are the 0th and 9th samples, and a total of 10 frames from 0 to 9 are inputted. Also, the results all display the 19th frame, which is 10 hours later.

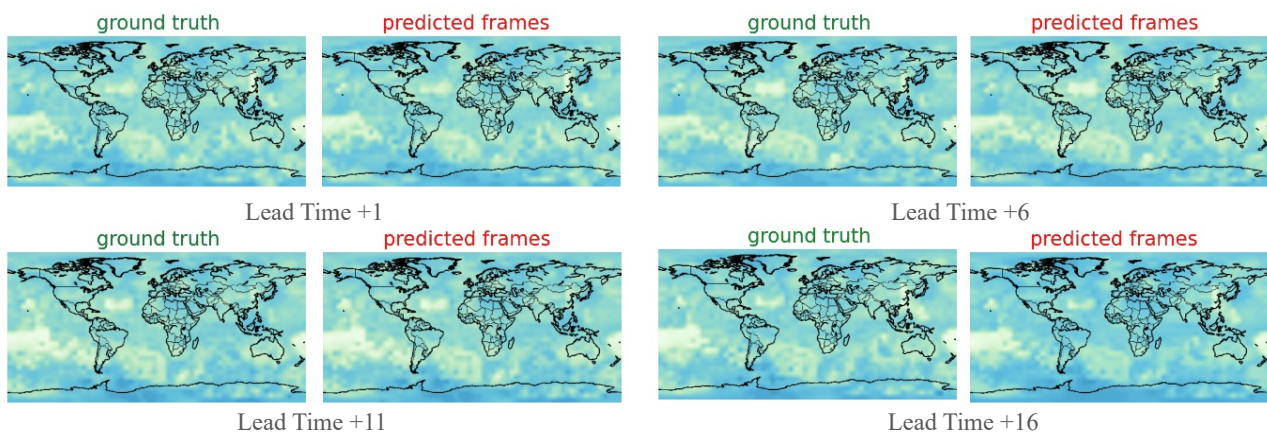


Figure 8. The qualitative results of DGDM from the WeatherBench dataset.